Multispectral optoacoustic tomography (MSOT) scanner for whole-body small animal imaging

Rui Ma, Adrian Taruttis, Vasilis Ntziachristos, and Daniel Razansky*

Institute for Biological and Medical Imaging, Technical University of Munich and Helmholtz Center Munich, Ingolstädter Landstraße 1, 85764 Neuherberg, Germany
**dr@tum.de*

Abstract: A major difficulty arising from whole-body optoacoustic imaging is the long acquisition times associated with recording signals from multiple spatial projections. The acquired signals are also generally weak and the signal-to-noise-ratio is low, problems often solved by signal averaging, which complicates acquisition and increases acquisition times to an extent that makes many *in vivo* applications challenging or even impossible. Herein we present a fast acquisition multispectral optoacoustic tomography (MSOT) scanner for whole-body visualization of molecular markers in small animals. Multi-wavelength illumination offers the possibility to resolve exogenously administered fluorescent probes, biomarkers, and other intrinsic and exogenous chromophores. The system performance is determined in phantom experiments involving molecular probes and validated by imaging of small animals of various scales.

OCIS codes: (170.5120) Photoacoutic imaging; (110.4234) Multispectral and hyperspectral imaging; (110.6880) Three-dimensional image acquisition; (170.3880) Medical and biological imaging; (120.3890) Medical optics instrumentation.

References and links

1. D. Razansky, M. Distel, C. Vinegoni, R. Ma, N. Perrimon, R. W. Koster, and V. Ntziachristos, "Multispectral opto-acoustic tomography of deep-seated fluorescent proteins in vivo," Nat. Photonics **3**(7), 412–417 (2009).
2. D. Razansky, C. Vinegoni, and V. Ntziachristos, "Multispectral photoacoustic imaging of fluorochromes in small animals," Opt. Lett. **32**(19), 2891–2893 (2007).
3. H. F. Zhang, K. Maslov, M. Sivaramakrishnan, G. Stoica, and L. H. V. Wang, "Imaging of hemoglobin oxygen saturation variations in single vessels in vivo using photoacoustic microscopy," Appl. Phys. Lett. **90**(5), 053901 (2007).
4. E. Z. Zhang, J. G. Laufer, R. B. Pedley, and P. C. Beard, "In vivo high-resolution 3D photoacoustic imaging of superficial vascular anatomy," Phys. Med. Biol. **54**(4), 1035–1046 (2009).
5. X. D. Wang, Y. J. Pang, G. Ku, X. Y. Xie, G. Stoica, and L. V. Wang, "Noninvasive laser-induced photoacoustic tomography for structural and functional in vivo imaging of the brain," Nat. Biotechnol. **21**(7), 803–806 (2003).
6. A. A. Oraevsky, V. A. Andreev, A. A. Karabutov, R. D. Fleming, Z. Gatalica, H. Singh, and R. O. Esenaliev, "Laser optoacoustic imaging of the breast: detection of cancer angiogenesis," Proc. SPIE **3597**, 352 (1999).
7. H. F. Zhang, K. Maslov, G. Stoica, and L. V. Wang, "Functional photoacoustic microscopy for high-resolution and noninvasive in vivo imaging," Nat. Biotechnol. **24**(7), 848–851 (2006).
8. Z. Yuan, and H. B. Jiang, "Simultaneous recovery of tissue physiological and acoustic properties and the criteria for wavelength selection in multispectral photoacoustic tomography," Opt. Lett. **34**(11), 1714–1716 (2009).
9. D. Razansky, J. Baeten, and V. Ntziachristos, "Sensitivity of molecular target detection by multispectral optoacoustic tomography (MSOT)," Med. Phys. **36**(3), 939–945 (2009).
10. E. Zhang, J. Laufer, and P. Beard, "Backward-mode multiwavelength photoacoustic scanner using a planar Fabry-Perot polymer film ultrasound sensor for high-resolution three-dimensional imaging of biological tissues," Appl. Opt. **47**(4), 561–577 (2008).
11. F. Helmchen, and W. Denk, "Deep tissue two-photon microscopy," Nat. Methods **2**(12), 932–940 (2005).
12. R. Yuste, "Fluorescence microscopy today," Nat. Methods **2**(12), 902–904 (2005).
13. American National Standards for the Safe Use of Lasers, ANSI Z136.1, American Laser Institute (2000).
14. G. Ku, X. D. Wang, G. Stoica, and L. V. Wang, "Multiple-bandwidth photoacoustic tomography," Phys. Med. Biol. **49**(7), 1329–1338 (2004).
15. R. A. Kruger, P. Liu, Y. R. Fang, and C. R. Appledorn, "Photoacoustic ultrasound (PAUS)--reconstruction tomography," Med. Phys. **22**(10), 1605–1609 (1995).

#117833 - $15.00 USD Received 28 Sep 2009; revised 23 Oct 2009; accepted 27 Oct 2009; published 9 Nov 2009

16. B. A. J. Angelsen, *Ultrasound imaging - Waves, Signals, and Signal Processing* (Emantec, Trondheim, 2000).
17. D. Razansky, and V. Ntziachristos, "Hybrid photoacoustic fluorescence molecular tomography using finite-element-based inversion," Med. Phys. **34**(11), 4293–4301 (2007).
18. T. Jetzfellner, D. Razansky, A. Rosenthal, R. Schulz, K. H. Englmeier, and V. Ntziachristos, "Performance of iterative optoacoustic tomography with experimental data," Appl. Phys. Lett. **95**(1), 013703 (2009).
19. Z. Yuan, and H. B. Jiang, "Quantitative photoacoustic tomography: Recovery of optical absorption coefficient maps of heterogeneous media," Appl. Phys. Lett. **88**(23), 231101 (2006).
20. A. Rosenthal, D. Razansky, and V. Ntziachristos, "Quantitative optoacoustic tomography using sparse signal representation," IEEE Trans. Med. Imag., DOI: 10.1109/TMI.2009.2027116 (2009).
21. C. Vinegoni, C. Pitsouli, D. Razansky, N. Perrimon, and V. Ntziachristos, "In vivo imaging of Drosophila melanogaster pupae with mesoscopic fluorescence tomography," Nat. Methods **5**(1), 45–47 (2007).
22. D. Razansky, C. Vinegoni, and V. Ntziachristos, "Imaging of mesoscopic-scale organisms using selective-plane optoacoustic tomography," Phys. Med. Biol. **54**(9), 2769–2777 (2009).
23. R. Weissleder, and V. Ntziachristos, "Shedding light onto live molecular targets," Nat. Med. **9**(1), 123–128 (2003).
24. N. Deliolanis, T. Lasser, D. Hyde, A. Soubret, J. Ripoll, and V. Ntziachristos, "Free-space fluorescence molecular tomography utilizing 360° geometry projections," Opt. Lett. **32**(4), 382–384 (2007).
25. K. V. Larin, I. V. Larina, and R. O. Esenaliev, "Monitoring of tissue coagulation during thermotherapy using optoacoustic technique," J. Phys. D Appl. Phys. **38**(15), 2645–2653 (2005).
26. J. Gamelin, A. Aguirre, A. Maurudis, F. Huang, D. Castillo, L. V. Wang, and Q. Zhu, "Curved array photoacoustic tomographic system for small animal imaging," J. Biomed. Opt. **13**(2), 024007 (2008).
27. R. A. Kruger, W. L. Kiser, D. R. Reinecke, G. A. Kruger, and K. D. Miller, "Thermoacoustic molecular imaging of small animals," Mol. Imaging **2**(2), 113–123 (2003).
28. R. J. Zemp, L. Song, R. Bitton, K. K. Shung, and L. V. Wang, "Realtime Photoacoustic Microscopy of Murine Cardiovascular Dynamics," Opt. Express **16**(22), 18551–18556 (2008).

1. Introduction

Multispectral optoacoustic tomography (MSOT) is a method capable of resolving chromophoric and fluorescent agents with molecular specificity through several millimeters to centimeters of tissue [1, 2]. The technique is based on the optoacoustic phenomenon, i.e. the generation of acoustic waves due to thermoelastic expansion caused by absorption of ultra-short optical pulses. Over the last decade optoacoustics has been considered for tissue imaging, mainly for resolving vascular contrast and the corresponding physiological changes, in particular oxy- and deoxy-hemoglobin [3], superficial vascular anatomy [4], brain lesion and functional cerebral hemodynamic changes [5], cancer angiogenesis [6], blood volume and oxygen consumption changes and the associated dynamic and functional neuronal activities [7]. The introduction of endogenous or exogenous reporter agents with molecular specificity, such as fluorescent proteins and probes, further allows the propagation of this technique towards molecular imaging applications. In this case a promising approach is the use of multispectral illumination in order to differentiate specific spectral signatures of key reporter agents over the background tissue absorption [1,2,8–10]. Combined, imaging of physiological and molecular markers using optoacoustics has the potential to achieve high resolution photonic imaging, through depths that go significantly beyond the capabilities of modern microscopy [11,12].

To perform molecular imaging of tissues and small biological organisms using MSOT, we developed an experimental prototype that is capable of multi-slice whole-body imaging. In contrast to many previous optoacoustic imaging studies that assumed plane illumination and homogenous light distribution within appropriately selected superficial sections of tissue [4,5,7], this system employs multi-angle side illumination of the entire volume of interest. A major difficulty arising from optoacoustic imaging, especially when considering whole-body small animal imaging applications, is the need for a large dynamic range to capture signals generated in deep regions and the corresponding long acquisition times associated with recording signals from multiple spatial projections with sufficient signal-to-noise ratio (SNR), after averaging. This might impose severe limitations on imaging of some dynamic and longitudinal phenomena that require good temporal resolution, such as dynamic bio-distribution of contrast agents, cell tracking, blood oxygenation monitoring etc. To address this aspect we introduce herein a time-efficient continuous data acquisition method and

#117833 - $15.00 USD Received 28 Sep 2009; revised 23 Oct 2009; accepted 27 Oct 2009; published 9 Nov 2009

demonstrate fast 360° data collection with sufficient SNR, without signal averaging. The method is showcased using a single cylindrically focused ultrasound detection element, but it is also appropriate for use with simultaneous multiple-element acquisition. The performance of the system developed is examined with tissue-mimicking phantom experiments and imaging of intact organisms of various sizes.

2. Methods and materials

2.1 Experimental setup

A simplified scheme of the experimental setup is displayed in Fig. 1. A tunable optical parametric oscillator (MOPO-700 series, Newport Corp., Mountain View, CA), pumped by a Q-switched Nd:YAG laser (Quanta-Ray Lab-Series 190-30 Newport), operating at its third harmonic (355nm), provides multi-wavelength illumination. The pulse duration of the laser is less than 10 ns and the repetition rate is 30Hz. The output laser beam is manipulated using an iris, slits, cylindrical/spherical lenses, and diffusers in order to improve illumination uniformity and adapt the incident beam shape to the size of the particular imaged object or region of interest. A beam splitter divides the beam into two equal-intensity parts illuminating the object's surface from opposite directions through two transparent windows in the water tank. In this way, excitation conditions close to uniform illumination are achieved. The laser pulse fluence on the surface of imaged objects is kept under 20 mJ/cm^2 in order to meet laser safety standards [13]. Optoacoustic signals are acquired using ultrasound transducers with central frequencies and focal lengths suited to the size of the imaged object and the scale of the features of interest. For smaller objects, such as the Drosophila pupa and Zebrafish presented herein, a piezoelectric PZT transducer with a 15 MHz central frequency, 19.05 mm focal length and 13 mm element diameter (V319, Panametrics-NDT, Waltam, MA) is used; larger objects, such as mice and large tissue-mimicking phantoms, are imaged using a PZT transducer with a 3.5 MHz central frequency, 38.1 mm focal length and 13 mm element diameter (V382, Panametrics-NDT, Waltam, MA). The transducers are cylindrically focused in the imaging plane to facilitate 2D image acquisition.

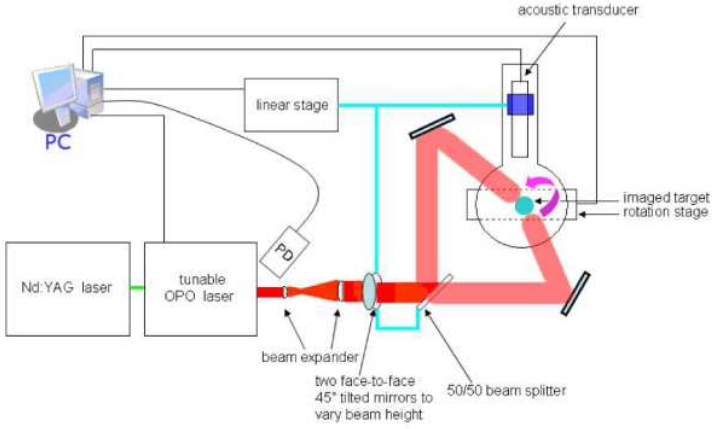

Fig. 1. Diagram of the multispectral optoacoustic tomography setup.

Two 45° tilted mirrors are used to change the beam height by moving the bottom mirror with a vertical translation stage. The beam splitter and the ultrasonic transducer are translated by the same stage, thus both the illumination and detection planes are translated simultaneously to allow for multi-slice image acquisition via vertical scanning. The sample is mounted on a rotational stage located at the bottom of the water tank while a sealed bearing (Isomag Corporation, Los Angeles, CA) is used to isolate the water-containing area from the

#117833 - $15.00 USD Received 28 Sep 2009; revised 23 Oct 2009; accepted 27 Oct 2009; published 9 Nov 2009

stepper motor located underneath the tank. In-plane data acquisition is done by 360° rotation of the sample. This arrangement ensures a compact design as only a small number of necessary components are located inside the water tank. A 14-bit resolution PCI digitizer with a sampling rate of 100 MS/s (NI PCI-5122, National Instruments Corp., Austin, TX) is used to record time-resolved acoustic signals from the detector. The laser, stages, and data acquisition are controlled via a Labview-based interface (National Instruments Corp., Austin, TX). In addition, a photodiode (FDS010, 200-1100 nm, 1 ns rise time, Thorlabs, Newton, NJ) is positioned in the vicinity of the laser output window to record the intensity change of each pulse and normalize the detected signals for laser output instabilities. The readings from the photodiode are calibrated with wavelength-dependent sensitivity curves provided by the manufacturer. This continuous power monitoring is of critical importance for multispectral reconstructions since many important molecular imaging agents may present only a small variation of the optical absorption over highly absorbing background, in which case even small quantification inaccuracies may lead to uninterpretable results.

2.2 Continuous data acquisition

The commonly applied optoacoustic acquisition loop [5, 14, 15] includes moving a stepper motor to an arranged position, detecting time-resolved signals, averaging them to attain the necessary SNR, saving the data and moving to the next angular projection or step. Here we employ instead a continuous data acquisition method, for which the rotation stage is accelerated to a predefined speed (depending on the number of projections to be acquired) and continuously moves for the entire 360° revolution. Low pulse-to-pulse jitter of the laser (<2 ns) provides good positioning accuracy. For validation of reconstruction accuracy, exact stage positions for the initial and last angular projection are recorded. The signals are acquired and stored for every laser pulse without averaging. If more signals are required for better *SNR*, the rotation speed is reduced so that more projections can be acquired. Compared to averaging methods, the continuous acquisition significantly cuts on acquisition times and allows recording of a greater number of information-containing projections, which also largely reduces reconstruction artifacts due to incomplete projection data.

In a more quantitative manner, the signal-to-noise ratio of the final reconstructed image can be written as $SNR \sim S \cdot \gamma \cdot A \cdot \sqrt{P \cdot M} / N$, where *S, γ, A, P, M,* and *N* are optoacoustic signal intensity, ultrasonic detector sensitivity, its area, number of projections (or detection elements in a multi-element array solution), number of signal averages, and noise floor of the system, respectively. In order to achieve higher *SNR*, it is always better to increase the magnitude of the generated optoacoustic signals, detector's sensitivity or its area rather than try to recover the signals via signal averaging. This also explains why it is not always possible to significantly cut on the acquisition times using multi-element detection solution, in which the signals are acquired simultaneously from multiple projections. Since the latter solution will usually employ a large number of small-area detectors, one might have to perform an extensive signal averaging to recover the *SNR*. However, the resulting SNR will be reduced as a function of an individual detector's area while it will only increase as a square root of the number of simultaneously detecting elements or signal averages. This fact might drastically reduce or even completely diminish the time gain of simultaneous multi-element signal acquisition as compared to solution having a single mechanically-translated detector with large area.

In order to validate the suggested continuous acquisition method, it is important to calculate the image blur resulting from moving the imaged object during data acquisition. For the simplified acquisition scheme, shown in Fig. 2, the laser repetition rate is 30 Hz, hence the time interval between two successive projections is ~33 ms. For the fastest possible rotation speed available in the current setup (6.7 RPM), corresponding to 270 projections over a full 360° rotation, the 2D image is acquired in 9 seconds. The object is therefore rotating with an

#117833 - $15.00 USD Received 28 Sep 2009; revised 23 Oct 2009; accepted 27 Oct 2009; published 9 Nov 2009

angular speed of 40 °/s. For a typical diameter of the imaged object of 2 cm and speed of sound of 1500 m/s, it will only take approximately 13 μs to record all the optoacoustic signals originating from the object. During this time, the maximal displacement of points within the object with respect to the transducer's surface can reach the value of approximately 0.1 μm, which is significantly smaller than the ultrasonic resolution that can be achieved, meaning that its blurring effects on the image can be safely neglected.

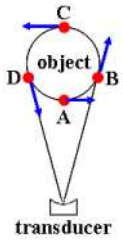

Fig. 2. Schematic representation of the continuous acquisition method and four important points concerning Doppler effect.

Nevertheless, when the imaged object is rotating, one should also take into account the Doppler effect caused by the object's motion relative to the transducer. When the acoustic source is moving with velocity v at an angle θ relative to the direction from the transducer to the acoustic source, the relative frequency shift in the acoustic signal can be calculated by [16]

$$\frac{\Delta f}{f} = \frac{v \cos\theta}{c} \tag{1}$$

where v is positive when the source is moving away from the transducer and negative when it moves towards the transducer. From the previous calculation, the maximal angular speed of 40 °/s corresponds to a linear speed of v = 6.98 mm/s on the surface of a 2 cm diameter object. In Fig. 2, $\theta = 90°$ at points A and C, and as a result the frequency of the detected acoustic wave has no Doppler effect. At points B and D the relative frequency shift reaches its maximum of approximately 0.0005%, or 50 Hz for 10 MHz frequency components, a value which is again negligible for the considered object size range.

We further note that typical tunable nanosecond lasers are generally unstable in terms of pulse energy, which can deviate by 20% and more between individual pulses. Clearly, when signal averaging is applied, acoustic signal fluctuations due to laser intensity instability are greatly reduced. In the continuous acquisition mode, however, the individual projections are not averaged, therefore pulse energy variations may introduce artifacts into the reconstructed optoacoustic images. To account for these effects we utilize the photodiode circuit described in the previous section for post-processing correction for pulse-to-pulse energy variations.

2.3 Reconstruction algorithm

The inversion algorithm used in image acquisition has been previously described [17], but is briefly explained here for completeness. The photoacoustic effect refers to the generation of broadband acoustic waves by absorption of short light pulses in matter. Under conditions of thermal confinement, i.e., when the light pulse is short enough so that thermal diffusion is insignificant during the pulse, the relationship between the pressure $p(\vec{r},t)$ and temperature $T(\vec{r},t)$ at time t and position $\vec{r}$ due to an incident light intensity $I(\vec{r},t)$ in W/m^2, can be expressed as,

#117833 - $15.00 USD Received 28 Sep 2009; revised 23 Oct 2009; accepted 27 Oct 2009; published 9 Nov 2009

$$\nabla^2 p(\vec{r},t) - \frac{1}{v_s^2}\frac{\partial^2 p(\vec{r},t)}{\partial t^2} = -\rho_m \beta \frac{\partial^2 T(\vec{r},t)}{\partial t^2} = -\frac{\beta \mu_a}{C}\frac{\partial I(\vec{r},t)}{\partial t} \quad (2)$$

where v_s, ρ_m, β, C and μ_a are speed of sound, mass density, isobaric volume expansion, specific heat and optical absorption coefficients of the medium, respectively. A point detector at position *r'* will sense an integrated pressure wave, which is the solution of Eq. (2), i.e.

$$p(\vec{r}',t) = \frac{\beta \mu_a}{4\pi C}\int_v \frac{\partial I(\vec{r},t')}{\partial t'}\frac{d^3\vec{r}}{\left|\vec{r}-\vec{r}'\right|}\Big|_{t'=t-\left|\vec{r}-\vec{r}'\right|/v_s} \quad (3)$$

For reconstruction of the optoacoustic source distribution from the measured acoustic pressures $p(\vec{r}',t)$, an explicit back-projection formula can be applied [15], that relates the measured acoustic pressure $p(\vec{r}',t)$ in an arbitrary scanning geometry S' to a optoacoustic source distribution $p_s(\vec{r})$ within the imaged object as

$$p_s(\vec{r}) = \frac{1}{2\pi}\iint_{S'} \frac{\overline{t}\,\partial p(\vec{r}',\overline{t})/\partial \overline{t} - p(\vec{r}',\overline{t})}{\left|\vec{r}-\vec{r}'\right|^3}\hat{n}'\cdot(\vec{r}-\vec{r}')dS'\Big|_{\overline{t}=\left|\vec{r}-\vec{r}'\right|} \quad (4)$$

where $\hat{n}'$ is a vector pointing outwards and normal to the closed surface S'. In our particular cylindrical scanning geometry, where the detector is focused in the imaging plane, we apply Eq. (4) in its reduced two-dimensional form, whereas, as mentioned, whole-body imaging is achieved by combining all reconstructed 2D images by scanning the illumination-detection plane in the vertical direction.

It is further noted that the initial optoacoustic image, reconstructed using Eq. (4) only represents a map of energy deposition in tissue rather than the absorption coefficient image, which corresponds to the actual distribution of optical absorbers. In other words, the image reconstructed is a product of the optical absorption coefficient and the local light fluence $U(\vec{r})$ within the tissue, i.e.

$$\mu_a(\vec{r})U(\vec{r}) = \frac{C}{\beta v_s^2}p_s(\vec{r}) \quad (5)$$

Thus, targets in deep tissue may appear weaker than targets having similar optical absorption but located close to the illuminated surface. Several methods have been recently suggested for quantitative extraction of the optical absorption in non-uniform illumination configurations, including iterative approaches [18,19], sparse signal decomposition [20], and analytical normalization [17]. The latter approach was adopted in this work mainly due to its simplicity.

2.4 Phantom preparation and imaging

To evaluate the performance of the developed system, four turbid tissue-mimicking cylindrical phantoms labeled Ph1, Ph2, Ph3 and Ph4, with optical properties as summarized in Table 1, were employed. Ph1-3 were made by molding 1.5% (by weight) of agar powder (Sigma-Aldrich, St. Louis, MO) mixed with 6% (by volume) of Intralipid-20% (Sigma-Aldrich, St. Louis, MO) to attain a reduced scattering coefficient of $\mu_s' = 10\ cm^{-1}$ and black India ink (Higgins, Sanford Bellwood, IL) for absorption. Hexagonal and round inclusions, with optical properties as in Table 1, were added to the phantoms. Ph4 was made of Polyvinyl chloride-plastisol (PVCP) with Titanium dioxide (TiO_2) powder and black plastic color (BPC) to introduce the necessary scattering and absorption [9]. Hydrophobic PVCP was used in order to hold solutions of fluorescent dyes, which tend to diffuse through agar phantoms. Ph1-Ph4 were imaged using the 3.5 MHz PZT transducer described in Section *2.1*. The background scattering and absorption properties of the phantoms were selected in the range of

#117833 - $15.00 USD Received 28 Sep 2009; revised 23 Oct 2009; accepted 27 Oct 2009; published 9 Nov 2009

typical mouse tissue optical properties at the imaged wavelengths [9]. In addition, a clear agar cylinder containing 10 µm diameter black-dyed polystyrene microspheres (Polysciences, Inc., Warrington, PA) at an approximate concentration of 20 spheres per ml was prepared to determine the spatial resolution of the system.

Table 1. Optical properties of the phantoms used for experimental validation.

Parameters \ Label	Ph1	Ph2	Ph3	Ph4
Diameter (mm)	14	16	28.5	17
μ_s' background (cm^{-1})	10	10	10	20
μ_a background (cm^{-1})	0.2	0.6	0.8	0.15
μ_s' insertion/s (cm^{-1})	10	10	10	20
μ_a insertion/s (cm^{-1})	1	3	8	2*
* 5µM Texas Red was added to one of the insertions.				

2.5 Animal imaging

The purpose of the animal imaging studies here was to provide verification of the main system performance characteristics, e.g. spatial resolution, on a variety of realistic targets of different sizes. We imaged two intact model organisms in the mesoscopic diffusion size range [21,22], i.e. a Drosophila melanogaster pupa and 1-year old adult Zebrafish *post mortem*. Both were imaged using the 15 MHz PZT transducer described in *2.1* in order to resolve their relatively small features. These organisms have both significant scattering and relatively small size that prevents them from being visualized using any of the existing microscopic [11, 12] or macroscopic (diffusion-based) [23] optical tomography techniques. The organisms were either partially or fully embedded into clear agar cylinders for simple handling and tomographic rotation. The typical diameter of a Drosophila melanogaster pupa is approximately 800 µm and the case is very scattering and absorbing. We acquired optoacoustic data from a pupa in the region of the salivary glands at 650 nm using the selective-plane illumination technique [22]. An adult Zebrafish has a cross-sectional diameter of approximately 6 mm and is also optically diffuse. Here, a wavelength of 605 nm was used for illumination.

Finally, we imaged the thorax and neck regions of an intact nude mouse *post mortem*. Compared to the smaller objects we have imaged so far, mice are large enough to be imaged by diffusion-based optical tomography techniques, however the scattering of light degrades spatial resolution at larger penetration depths when using these methods, a disadvantage readily overcome by optoacoustic tomography. In order to achieve a high sensitivity for the relevant feature sizes and allow for a sufficient focal length, the imaging was performed with the 3.5 MHz PZT transducer described in Section *2.1*. The illumination wavelength was 730 nm, a point where tissue absorption is relatively low, thus allowing deep penetration. Although the mouse imaged here was sacrificed before the experiment, the geometry of the measurement setup allowed for the mouse to be positioned upright in the water chamber with its snout above the water while the rest of the body was immersed, thus providing the capability of *in vivo* imaging.

3. Results

3.1 Spatial resolution of the system

To determine the spatial resolution of the system we used the 15 MHz PZT transducer described in *2.1* to image the microsphere-containing agar cylinder described in *2.4*. The inset of Fig. 3(a) shows a reconstructed 2D image of a microsphere. In Fig. 3(a), the plotted signal intensity across the image indicates a FWHM (full width at half maximum) of 42 µm, which gives us an in-plane resolution of 32 µm when taking into account the size of the

#117833 - $15.00 USD Received 28 Sep 2009; revised 23 Oct 2009; accepted 27 Oct 2009; published 9 Nov 2009

microspheres. This value corresponds well to the available detection bandwidth of the transducer (up to ~20 MHz).

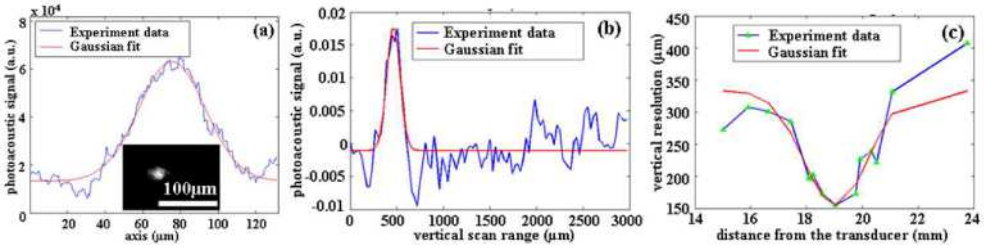

Fig. 3. (a) In-plane resolution measurements of cylindrically-focused PZT transducer with center frequency of 15 MHz using 10 μm microsphere suspension, attaining an in-plane resolution of 32 μm, inset: optoacoustic image of a microsphere; (b) Vertical scan through a microsphere located 19.035mm in front of the transducer. Vertical resolution of ~155 μm is derived for this distance. The distance is calculated via time-of-flight method, and the figure is obtained by vertically scanning the phantom and recording acoustic signal coming from the same distance. The blue curve indicates the measured signal intensity variations and the red line is the Gaussian fit; (c) Vertical resolution dependence on the distance between the imaged object and the transducer.

To determine the vertical resolution, we scanned the transducer vertically along the cylinder embedded with microspheres for 100 steps with 30 μm step size. Within these 100 steps, many microspheres, located at different distances from the transducer, were detected. By tracking and plotting the magnitude of optoacoustic response for each microsphere in consecutive imaging planes, calculating the corresponding distances to the transducer's surface and subsequently applying a Gaussian fit, one can derive the vertical resolution map for the cylindrically focused detector. In this way, an approximate length of the focal zone can also be determined. Figure 3(b) shows signal magnitudes obtained for a vertical scan through a sphere located close to the focus, attaining a vertical resolution of ~155μm, which agrees well with the transducer specification. Figure 3(c) shows the vertical resolution dependence on the distance between the imaged object and the transducer, from which we deduce an effective focal zone length of 2.7 mm, defined by the FWHM of a Gaussian fit. As can be seen from the curve, the best vertical resolution corresponds to the specified focal length of the transducer (19.05 mm).

3.2 Turbid phantom images

The turbid phantoms Ph1 and Ph2 were imaged using continuous acquisition and compared with acquisition using signal averaging. Figure 4(a) and 4(b) show optoacoustic images of Ph1 using continuous and averaged acquisition, respectively. The former uses 270 angular projections without averaging and the latter 90 projections with 32 averages per projection. The quality of the reconstructed images for both acquisition methods look similar, however, in continuous acquisition mode it took approximately 9 seconds to acquire the 2D image while the acquisition time with averaging was 200 seconds. In this case, with similar image quality, continuous acquisition took only 1/22 of the time required for averaging mode.

Figure 4(c) and 4(d) show the resulting images from the two acquisition methods for Ph2. Here 960 projections were used for the continuous acquisition and 20 projections with 32 averages each for the averaging method so that both methods have a similar acquisition time (about 35 seconds per 2D slice). However, the continuous acquisition image has significantly better quality and is free of the arc-like artifacts resulting from the averaged acquisition with too few projections.

#117833 - $15.00 USD Received 28 Sep 2009; revised 23 Oct 2009; accepted 27 Oct 2009; published 9 Nov 2009

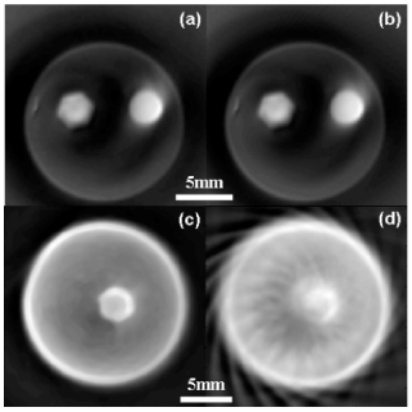

Fig. 4. (a) Cross-sectional optoacoustic image of Ph1 acquired in continuous acquisition mode with 270 angular projections; (b) reconstruction of Ph1 in averaged acquisition mode with 90 projections and 32 averages per projection; (c) reconstruction of Ph2 in continuous acquisition mode with 960 projections; (d) reconstruction of Ph2 in averaged acquisition mode with 20 projections and 32 averages per projection.

To simulate imaging of deep-seated targets in a very absorbing tissue-like medium, Ph3 was used with a diameter of 28.5mm [Fig. 5(a)]. It was made with a background optical absorption coefficient of μ_a = 0.8 cm^{-1}, which is approximately four times higher than average mouse tissue absorption at the imaging wavelength of 650 nm. Figure 5(b) shows optoacoustic reconstructions of Ph3 acquired at 650nm containing a hexagonal insertion at a depth of more than 1 cm, which is clearly visible in the images with high resolution and SNR. Figure 5(c) shows a magnified view of the insertion from the image in Fig. 5(b). The calculated SNR of the image in Fig. 5(c) is 22.25 dB, where the green and magenta labeled regions represent signal and background respectively. The system has therefore been clearly demonstrated to have the capability of imaging deep tissue contrast within large objects with relatively high background absorption.

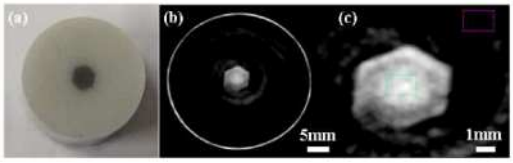

Fig. 5. (a) Photograph of Ph3 with diameter of 28.5 mm; (b) Optoacoustic reconstruction of Ph3 acquired at 650nm; (c) Magnified image around the insertion. SNR is calculated from the green and magenta labeled regions, representing signal and background respectively.

3.3 Animal imaging

The image of the Drosophila pupa, shown in Fig. 6(a), clearly reveals the anatomical details of the animal, i.e. the absorbing case, two low absorbing salivary glands and the rest of the volume filled with fatty structures. Since the case of the pupa is very thin (typically less than 10 μm), it can be used to verify the spatial resolution of the system (with the particular PZT detector used) in a real biological imaging scenario. As can be seen in Fig. 6(b), the case thickness is translated into ~43 μm (FWHM) in the optoacoustic image, which, assuming an actual case thickness of approximately 10 μm, gives an in-plane resolution of ~33 μm, in good agreement with the value obtained in Section *3.1*. Similarly, the cross-sectional Zebrafish image in Fig. 6(c) further demonstrates the high contrast and resolution capability of the system and correlates well with the corresponding histological slice shown in Fig. 6(d).

#117833 - $15.00 USD Received 28 Sep 2009; revised 23 Oct 2009; accepted 27 Oct 2009; published 9 Nov 2009

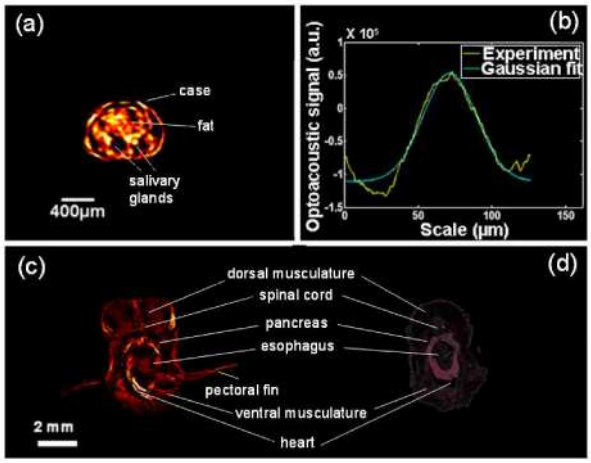

Fig. 6. (a) Optoacoustic image of intact drosophila pupa; (b) One-dimensional cut through the reconstructed image in (a) for verification of in-plane resolution; (c) Cross-sectional optoacoustic image of an intact 1- year old adult Zebrafish; (d) Corresponding histological slice made through a sacrificed Zebrafish specimen.

Figure 7 shows transverse optoacoustic images taken at three heights through the thorax and neck of a nude mouse, with corresponding CT images using a blood contrast agent (eXIA 160, Binitio Biomedical, Ottawa, Canada).

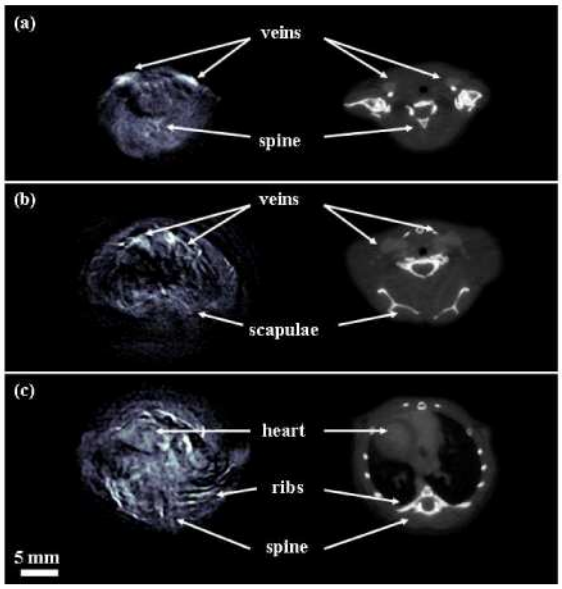

Fig. 7. Transverse optoacoustic images (left) from the thorax and neck regions of a nude mouse with corresponding CT images (right) using a blood contrast agent. The images were acquired at three different heights on the mouse: (a) was acquired at the top of the shoulders, (b) through the scapulae, and (c) at the height of the heart. Prominent features visible on both the optoacoustic and CT images are labeled.

In Fig. 7 features such as blood vessels, spinal structures, the heart, and ribs can be found in both the optoacoustic and CT images. Differences in the images can be explained by the differing contrast mechanisms of the two modalities, the significant difference in vertical resolution between 2D optoacoustic tomography using a cylindrically focused transducer and CT, and effects on the shape of the mouse caused by different positioning in the optoacoustic

#117833 - $15.00 USD Received 28 Sep 2009; revised 23 Oct 2009; accepted 27 Oct 2009; published 9 Nov 2009

system compared to the CT machine. As can be qualitatively assessed from the optoacoustic images, high resolution is maintained deep inside the mouse.

3.4 Molecular probe detection

As described in Section *2.4*, Ph4 was used to demonstrate system's molecular probe detection sensitivity. For this, the phantom was embedded with a solution containing a common fluorescent dye, Texas Red (peak excitation 596 nm; peak emission 615 nm) at 5 μM concentration. The dye was in an already highly absorbing solution of ink having $\mu_a = 2\text{cm}^{-1}$, which was selected in order to simulate the realistic case of a fluorescent imaging agent located in whole blood. We employed continuous data acquisition to obtain optoacoustic images at the peak excitation wavelength of Texas Red (596nm) and at 612nm where its absorption drops significantly [Fig. 8(a)-8(b)]. By subtracting optoacoustic images at these two wavelengths one can efficiently suppress the slowly varying background absorption and reveal the correct location of the Texas Red dye, as shown in Fig. 8(c).

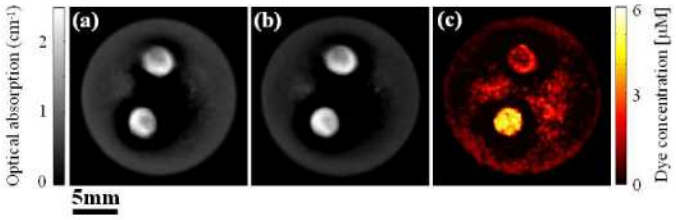

Fig. 8. Optoacoustic image of Ph4 acquired at (a) 596 nm and (b) 612nm. (c) Subtraction between 596nm and 612nm images revealing location of the Texas Red dye.

As can be seen, the subtraction process reduces background signals coming from both insertions containing the highly absorbing ink solution and from the background of the phantom as well. We calculated the Contrast-to-noise ratio (CNR) of the multispectral image using the following formula:

$$CNR = \frac{S_{Dye} - S_B}{\sigma} \tag{6}$$

where S_{Dye} is the averaged value of dye signal obtained after wavelength subtraction [Fig. 8(c)], S_B is the averaged value of the background after wavelength subtraction, and σ is the standard deviation of S_B. The calculated SNR and CNR in Fig. 8(c) were 25.17 and 16.87, respectively, which translates to a noise floor equivalent dye concentration of ~300 nM. This translates to an amount of 12 femtomoles of the dye that was detected in each resolution-limited voxel of the 3.5 MHz PZT transducer (~0.2 x 0.2 x 1 mm). However, in our phantom experiment, the actual optoacoustic signals were recorded from a large amount of the dye contained in the insertion. As we have shown in [8], the detection sensitivity limits cannot therefore be linearly extrapolated using measurements performed on larger amounts of the probe. A more accurate analysis based on the methodology described in [8], which takes into account optical properties, size and depth of the target as well as light and acoustic attenuation, will lead to detection limits on the order of several hundreds of femtomoles for the current experimental setup and phantom properties. Clearly, in realistic animal experiments, additional factors, such as absorption inhomogeneities, acoustic mismatches, movement artifacts and other issues related to in-vivo imaging, will adversely affect image quantification and sensitivity limits. There we expect for sensitivity limits in the few picomoles range, similar to what is achievable with state-of-the-art fluorescent molecular tomography systems [24]. Finally, it has to be noted that, besides the particular optical properties of the imaged object and characteristics of the target probe, the absolute sensitivity

#117833 - $15.00 USD Received 28 Sep 2009; revised 23 Oct 2009; accepted 27 Oct 2009; published 9 Nov 2009

limits also greatly depend on a large number of other experimental and instrumentation-related parameters, such as laser energy, detector's sensitivity, number of averages/projections etc. With improvement of system performance, the practical sensitivity limits are expected to be well in the sub-picomole range, also for in-vivo experiments.

4. Discussion and conclusions

One difficulty arising from whole-body optoacoustic imaging is the long acquisition times associated with recording signals from multiple spatial projections. The acquired signals are also generally weak and the SNR is low, problems that are often solved by multiple averaging, which complicates the measurement and makes *in vivo* imaging challenging. To have a rough estimate on the order of magnitude of a typical optoacoustic disturbance, one can consider a simplified one-dimensional case of a short pulsed beam impinging on an absorbing half-space [25]. Under thermal confinement conditions, the pressure-rise distribution $p_s(\vec{r})$ can be expressed as,

$$p_s(\vec{r}) = \frac{\beta v_0^2}{C} \mu_a(\vec{r}) U(\vec{r}) \tag{7}$$

where typical parameters for biological tissue are $\beta = 3 \cdot 10^{-4}$ ($^\circ C^{-1}$) for the thermal expansion coefficient; $v_0 = 15 \cdot 10^4$ (cm s^{-1}) for the speed of sound; $C = 4.186$ (J g^{-1} $^\circ C^{-1}$) for the specific heat capacity at constant pressure; and $\mu_a = 0.3$ cm^{-1} for the optical absorption coefficient. In a typical imaging scenario, illumination of tissue with maximal permissible fluence of U = 20mJ/cm^2 [13] will only result in optoacoustic disturbances on the order of 1 kPa on the tissue surface light is incident upon, which will translate to an order of magnitude lower detectable pressure variations on the detector's surface. If deep tissue imaging is of interest, the pressure variations will be further affected by light attenuation and acoustic dispersions, which will bring the signals down by another order of magnitude and more, so that only few Pascals are available for detection. Finally, when considering multispectral optoacoustic tomography (MSOT) data acquisition [1], in which the same tomographic data is recorded at several different wavelengths, whole-body image acquisition times might become unrealistic. Additional considerations arise from the requirement for high resolution and quality optoacoustic tomographic reconstructions that directly correspond to the detection bandwidth, which should ideally be as large as possible. For this, one could use ultrawideband ultrasound detection technologies, such as pVDF film detectors [17] or Fabry-Perot interferometric approaches that have already proven to be a potential tool for high-resolution optoacoustic imaging *in vivo* [4, 10]. However, compared to these broadband approaches, PZT and other piezocomposite technologies can normally provide higher SNR and robustness, at the cost of narrower bandwidth.

In tomographic applications, for attaining the best quality quantified reconstructions, the optoacoustic responses have to be collected from as many locations as possible around the imaged object or region of interest. To cut on acquisition times, one could possibly use multiple detectors (ultrasound array) to simultaneously record the outgoing signals, as in [26–28]. Having multiple simultaneous detectors is, however, a costly and technologically challenging option. Furthermore, multi-element detection solution will usually force one to use small area elements. Therefore, due to signal-to-noise ratio considerations (as discussed in Section 2.2), it might fail to achieve a significant improvement in the acquisition times. Our single element solution allows to use highly sensitive (large-area) interchangeable transducers and offers therefore a good compromise between acquisition speed, complexity and noise performance.

The presented fast-acquisition multispectral optoacoustic tomography system for whole-body imaging of small animals enables compact tomographic design by using sealed bearing that effectively isolates liquid area from the rotation driving parts. The scanner provides a

#117833 - $15.00 USD Received 28 Sep 2009; revised 23 Oct 2009; accepted 27 Oct 2009; published 9 Nov 2009

variety of optical means for optimal adjustment of sample excitation. This offers the flexibility required for imaging at different object dimension scales, from organisms like Drosophila pupa (diameter below 1 mm) up to larger animals and samples with characteristic sizes of few centimeters and more. The two-way illumination configuration is adopted for attaining approximate uniformity in object's illumination, which is crucial for high quality quantitative image reconstruction. To speed up the acquisition process, we employ a continuous acquisition methodology, for which the object is rotating constantly during data acquisition, a method that was shown to save up to one order of magnitude in typical acquisition times.

In its current implementation, the scanner is capable of acquiring a single wavelength 2D image in approximately 9 seconds using a single cylindrically-focused ultrasonic detector, which corresponds to acquisition times of about 20 minutes for typical whole-body multi-wavelength data acquisition using 40 vertical slices and 3 wavelengths. A cylindrically focused element is used here in order to increase detection area and sensitivity, in exchange for compromising image quality and resolution along dimensions where focusing is performed. The best in-plane and vertical spatial resolutions demonstrated in this study were 32 μm and 155 μm, respectively.

Furthermore, multi-wavelength illumination offers the possibility to resolve exogenously administered fluorescent probes or other chromophores. The simplest image subtraction approach, demonstrated here, works optimally with absorbers that offer a steep absorption (extinction) change, characteristic of fluorochromes. However, measurements at multiple wavelengths can provide further ability to simultaneously resolve multiple biomarkers, dyes and other intrinsic and exogenous chromophores.

Acknowledgment

D. R. acknowledges support from the German Research Foundation (DFG) Research Grant (RA 1848/1).

#117833 - $15.00 USD Received 28 Sep 2009; revised 23 Oct 2009; accepted 27 Oct 2009; published 9 Nov 2009